Textile & Leather Review

ISSN 2623-6281| www.tlr-journal.com | 10.31881/TLR

Novel Profile and Method of Design for Hydrogen Circulating Roots Pumps

Zhenxing Wu, Renyong Lin, Peihan Qi, Lingbo Zhang

How to cite: Wu Z, Lin R, Qi P, Zhang L. Novel Profile and Method of Design for Hydrogen Circulating Roots Pumps. Textile & Leather Review. 2026; 9: 2374-2405. https://doi.org/10.31881/TLR.2026.2374

How to link: https://doi.org/10.31881/TLR.2026.2374

Published: 25 April 2026

Novel Profile and Method of Design for Hydrogen Circulating Roots Pumps

Zhenxing Wu[1,2]*, Renyong Lin[2], Peihan Qi[1], Lingbo Zhang[2]

[1]College of Metrology Measurement and Instrument, China Jiliang University, Hangzhou 310018, Zhejiang, China

[2]Leo Group Pump (Zhejiang) Co., Ltd., Hangzhou 310018, Zhejiang, China

*wzx2022@cjlu.edu.cn

Article

https://doi.org/10.31881/TLR.2026.2374

Published 25 April 2026

ABSTRACT

Roots pumps play a crucial role in hydrogen fuel cell systems. As the textile industry seeks sustainable power solutions to achieve carbon neutrality in manufacturing, hydrogen energy has emerged as a promising alternative for clean energy supply. However, existing Roots pumps designs still fall short of delivering superior overall performance, i.e., the capability to achieve high volumetric efficiency and low flow pulsation simultaneously. This paper first summarizes the general design methodology and geometrical constraints for rotor profiles. Subsequently, a method for determining key design parameters from these geometrical constraints is proposed. Using this methodology, the circular arc rotor, hyperbolic rotor and parabolic rotor profiles are designed. In order to simultaneously meet the requirements for high volumetric efficiency and low flow pulsation, a novel profile composed of arc, parabolic, and their conjugate curve segments is proposed. Numerical simulations reveal that the proposed rotor achieves the highest volumetric efficiency and the lowest flow pulsation, demonstrating its potential for improving the performance of hydrogen circulation in fuel cell systems. Flow field analysis revealed that the intensity and scale of the vortices generated at the junction between the two rotor profiles are the root cause of flow pulsation.

KEYWORDS

textile industrial application, hydrogen circulating pump, new design formula, solution of design parameters, novel rotor profile

INTRODUCTION

The demand for highly stable and efficient fluid machinery is particularly pronounced in specialized sectors such as textile manufacturing. In modern textile machinery, such as high-speed spinning or weaving

equipment, the stability of the power and auxiliary systems directly dictates product quality [1,2]. Concurrently, energy-intensive industries like textile manufacturing are under growing pressure to reduce their carbon footprint by adopting greener manufacturing processes. In this context, hydrogen energy has emerged as a promising candidate for powering next-generation textile plants. Hydrogen fuel cell systems can provide the consistent and reliable power output essential for precision textile manufacturing [3,4].

Hydrogen fuel cell require a complex set of management systems to ensure that they work properly. These systems typically include hydrogen supply, oxygen supply, hydrothermal management, and electronic control units [5]. In hydrogen fuel cell systems, Roots pumps serve as critical components for hydrogen recirculation, ensuring a stable anode gas supply—and thus consistent power output—while also improving hydrogen utilization and alleviating anode flooding [6-8]. Therefore, a Roots pump design that minimizes flow pulsation and enhances volumetric efficiency is not only beneficial for general industrial use but also holds significant potential for improving the reliability of power systems in textile machinery and related hydrogen energy applications.

The rotor profile is a key factor influencing the performance of Roots pumps, as it directly affects volumetric effi-ciency and flow pulsation. Rotor clearance leakage is an important factor affecting the volumetric efficiencies of Roots pumps. To reduce leakage, researchers have developed various modifications to the traditional circular-arc profile, such as a profile consisting of five arc segments [9]; a profile consisting of two circular arcs, an involute, and the conjugate curve of the arcs [10]; a profile consisting of an arc, an external cycloid, an involute, and an envelope of the external cycloid [11]; a profile consisting of a conjugate curve of arcs, an external cycloid, an involute, and an encircled curve of the external cycloid and arcs [12]. However, studies have shown that rotor profiles modified based on elliptical arcs can increase the flow rate of Roots pumps and even reduce operational noise [13,14]. Furthermore, Hwang et al. [15] utilized an extended cycloidal rotor with a variable cycloid ratio to generate a new profile. This extended cycloid rotor achieves higher volumetric efficiency compared to conventional cycloidal rotors. Zhou et al. [8] proposed a profile composed of six curve segments, including a conjugate curve with three arcs, an involute, an external cycloid, and an arc. The new profile not only improves volumetric efficiency and flow rate but also enhances volumetric utilization.

In addition to the study of rotor profiles, researchers have also examined how clearance and operating parameters affect pump performance. Singh et al. [16] measured the optical velocity of a Roots pump using a fast camera, continuous particle image velocimetry and instantaneous image testing, respectively. Their results indicated that leakage flow en-hances turbulent mixing within the pump. Specifically, vortices generated by axial and inter-lobe leakage flows were identified as major contributors to this mixing effect. Numerous studies have shown that an increase in rotor clearance leads to a decrease in the volumetric efficiency of Roots pumps [17,18]. Zhou et al. [19] found that the increase in clearance helps to reduce the amplitude. They also concluded that a higher pressure ratio increases both the pressure pulsation amplitude and the leakage flow at the rotor-casing clearance, thereby reducing volumetric efficiency. Dong et al. [20] investigated the influence of rotational speed on a Roots pump. They found that higher rotational speeds reduce pressure pulsations and improve volumetric efficiency. However, they also found that an increase in speed increased the noise at the outlet. Li et al. [21] studied the impact of a high-pressure ratio on Roots pumps. Their results revealed that leakage flow driven by the pressure difference is a primary cause of flow disorder within the pump, with axial clearance leakage being the most severe.

Previous research has demonstrated that rotor profile, clearance, and operating parameters significantly influence the performance of Roots pumps. In general, hydrogen circulation pumps must achieve both high volumetric efficiency and low flow pulsation. However, existing Roots pumps often struggle to achieve optimal overall performance, and their rotor profile design methods are also characterized by homogenization and limited flexibility. Therefore, this paper first sum-marizes the general design methodology and geometrical constraints for rotor profiles. Subsequently, a method for de-termining key design parameters from these geometrical constraints is proposed. Using this methodology, the circular arc rotor, hyperbolic rotor and parabolic rotor profiles are designed. In order to simultaneously meet the requirements for high volumetric efficiency and low flow pulsation, a novel profile composed of arc, parabolic, and their conjugate curve

segments is proposed. This research addresses two key limitations: the lack of diversity in conventional Roots pump rotor profile design and the difficulty in resolving their geometrical constraints. Consequently, it provides a valuable reference for the development of high-performance Roots pumps.

ROTOR PROFILE DESIGN THEORY

Conjugate Curve

The profile of the rotor must be the conjugate curve, because it meets two basic conditions at any moment during the same speed of the two rotors: (1) the meshing point of the two rotors is unique, (2) the vector of the relative velocity of the two rotors in the direction of the common normal at the meshing point is zero. It should be noted that phase lag, which can occur during the assembly and operation of practical Roots pumps, may adversely affect pump performance. Mitigating phase lag necessitates strict tolerance control and the use of high-precision timing gears. However, the theoretical derivation in this paper is intended to establish a geometric foundation for the rotor profile; a detailed discussion of phase lag falls outside the scope of this study.

The most common method for knowing a two-dimensional curve and determining its conjugate curve is to establish three coordinate firstly, including two dynamic coordinates and one static coordinate, and then solve the problem by two-dimensional coordinate transformation with conjugate theory. Figure 1 shows that R is the radius of the base circle, P is the contact point of the rotor, XOY is the static coordinate, $X_1O_1Y_1$ and $X_2O_2Y_2$ are auxiliary coordinate, O is the tangent point of the two base circles and is on the X axis.

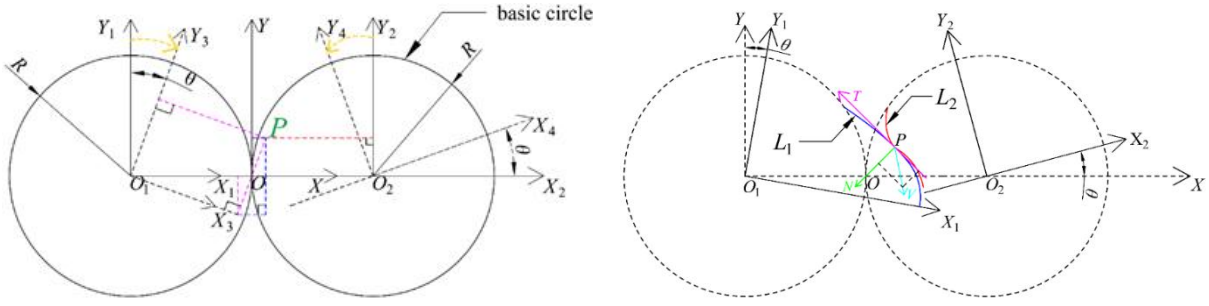

Figure 1. Derivation of conjugate curves. (a) coordinate transformation; (b) conjugate curve

We suppose that at a certain moment, when $X_1O_1Y_1$ rotates clockwise by an angle of ϑ and then becomes $X_3O_1Y_3$. The speeds of the two rotors are the same in opposite directions, so $X_2O_2Y_2$ is rotated counterclockwise by an angle of ϑ and becomes $X_4O_2Y_4$. It is useful to set the coordinates of point P in the

XOY、$X_1O_1Y_1$、$X_2O_2Y_2$、$X_3O_1Y_3$ and $X_4O_2Y_4$ coordinate as (x, y), (x_1, y_1), (x_2, y_2), (x_3, y_3), (x_4, y_4). According to the geometrical relations in Figure 1(a), the coordinates are obtained under:

$$\begin{cases} x_4 = x_3 \cos 2\theta + y_3 \sin 2\theta - 2R\cos\theta \\ y_4 = -x_3 \sin 2\theta + y_3 \cos 2\theta + 2R\sin\theta \end{cases} \tag{1}$$

Both $X_3O_1Y_3$ and $X_4O_2Y_4$ are obtained by rotating the auxiliary coordinate $X_1O_1Y_1$ and $X_2O_2Y_2$, respectively. Therefore, we get the transformation matrix:

$$A = \begin{bmatrix} \cos 2\theta & \sin 2\theta & -2R\cos\theta \\ -\sin 2\theta & \cos 2\theta & 2R\sin\theta \\ 0 & 0 & 1 \end{bmatrix} \tag{2}$$

A curve is composed of countless points, so the transformation of curve equations between different coordinate can be realized by matrix A. The parametric equation of the curve of L_1 is known to be:

$$L_1 = \begin{bmatrix} x_1(t) \\ y_1(t) \\ 1 \end{bmatrix} \tag{3}$$

Then the set of envelopes of the curve L_1 is L:

$$L = AL_1 \tag{4}$$

To determine the conjugate curve L from L_2, we analyze it by using the principle of meshing. According to the meshing principle, the line OP connecting the meshing point P, the point O is always the unit normal vector N of the two curves at the meshing point, as shown in Figure 1(b), and T is the tangent vector to the point P:

$$\begin{cases} \boldsymbol{T} = \dfrac{(\dfrac{\partial x_1(t)}{\partial t}, \dfrac{\partial y_1(t)}{\partial t})}{\sqrt{[\dfrac{\partial x_1(t)}{\partial t}]^2 + [\dfrac{\partial y_1(t)}{\partial t}]^2}} \\ \boldsymbol{N} = \dfrac{(\dfrac{\partial y_1(t)}{\partial t}, -\dfrac{\partial x_1(t)}{\partial t})}{\sqrt{[\dfrac{\partial x_1(t)}{\partial t}]^2 + [\dfrac{\partial y_1(t)}{\partial t}]^2}} \end{cases} \tag{5}$$

According to the conjugate theory, the velocity vector of the two rotors in the direction of the unit normal at the point of contact is zero, so it is also necessary to add the restriction [14,15]:

$$\begin{cases} \boldsymbol{N} \cdot \boldsymbol{V} = 0 \\ \boldsymbol{V} = (-2R\sin\theta + 2y_1, -2x_1 + 2R\cos\theta) \end{cases} \tag{6}$$

where *V* denotes the vector of relative velocity of the two rotors at the point of contact. When *N*·*V*=0, it means that the vector of the relative velocity of the two rotors in the common normal at the contact point is zero. According to Eq. (5) and Eq. (6) can be obtained:

$$\frac{\partial x_1(t)}{\partial t}\cos\theta + \frac{\partial y_1(t)}{\partial t}\sin\theta = \frac{1}{R}\left[y_1(t)\frac{\partial y_1(t)}{\partial t} + x_1(t)\frac{\partial x_1(t)}{\partial t} \right] \tag{7}$$

To solve for the relationship between ϑ and *t*, we can make the following assumptions:

$$\begin{cases} a = \dfrac{\partial x_1(t)}{\partial t}, \quad b = \dfrac{\partial y_1(t)}{\partial t} \\ c = \dfrac{1}{R}\left[y_1(t)\dfrac{\partial y_1(t)}{\partial t} + x_1(t)\dfrac{\partial x_1(t)}{\partial t} \right] \end{cases} \tag{8}$$

Substituting Eq. (8) into Eq. (7):

$$a\cos\theta + b\sin\theta = c \tag{9}$$

This can be obtained by using the auxiliary angle formula:

$$\begin{cases} \varphi = \arctan\dfrac{a}{b} \\ a\cos\theta + b\sin\theta = \sqrt{a^2+b^2}\,\sin(\theta + \arctan\dfrac{a}{b}) \end{cases} \tag{10}$$

In Eq. (10), φ is the auxiliary angle, and if φ is restricted to [0, π]:

$$\theta = \begin{cases} -\arctan\dfrac{a}{b} + \arcsin\dfrac{c}{\sqrt{a^2+b^2}} (b > 0) \\ \pi - \arctan\dfrac{a}{b} + \arcsin\dfrac{c}{\sqrt{a^2+b^2}} (b < 0) \end{cases} \tag{11}$$

Combining Eq. (3), Eq. (4) and Eq. (11) to obtain the conjugate curve L_2. Although the above derivation calculates the conjugate curve L_2, the position of L_2 and L_1 is incorrect, as shown in Figure 2(a). Because matrix A only solves for L_2, and does not connect L_2 and L_1 completely to form the rotor profile. Therefore, it is necessary to rotate L_2:

$$\begin{cases} \alpha = \dfrac{\pi}{2z} \\ \phi = 2\alpha - \pi \\ \boldsymbol{U} = \begin{bmatrix} \cos\phi & -\sin\phi & 0 \\ \sin\phi & \cos\phi & 0 \\ 0 & 0 & 1 \end{bmatrix} \\ L_2 = \boldsymbol{U}\boldsymbol{A}L_1 \end{cases} \tag{12}$$

where α is the rotor envelope angle, and z is the number of lobes. Eq. (12) connect L_1 and L_2 perfectly, as shown in Figure 2(b).

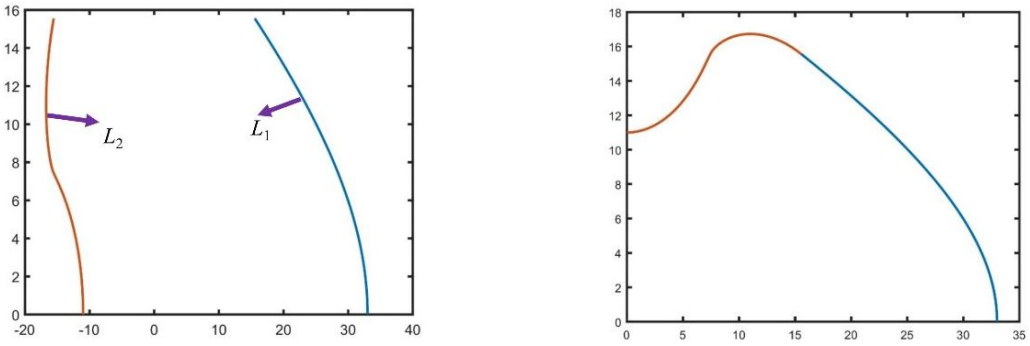

a) b)

Figure 2. (a) Unconnected curves; (b) Connected curves

In summary, when the equation of the curve L_1 is known, its conjugate curve L_2 can be determined by the following equation:

$$\begin{cases} L_2 = \boldsymbol{UA}L_1 = \begin{bmatrix} x_1(\mathrm{t})\cos(2\theta-\phi) + \mathrm{y}_1(t)\sin(2\theta-\phi) - 2R\cos(\theta-\phi) \\ x_1(t)\cos(2\theta+\phi) + y_1(t)\cos(2\theta-\phi) + 2R\sin(\theta-\phi) \\ 1 \end{bmatrix} \\ \phi = \dfrac{\pi}{z} - \pi, \quad a = \dfrac{\partial x_1(t)}{\partial t}, \quad b = \dfrac{\partial y_1(t)}{\partial t} \\ c = \dfrac{1}{R}\left[x_1(t)\cdot a + y_1(t)\cdot b\right], \quad \varphi = \arctan\dfrac{b}{a} \\ \begin{cases} \theta = \arcsin\left(\dfrac{c}{\sqrt{a^2+b^2}}\right) - \varphi, \ b > 0 \\ \theta = \pi + \arcsin\left(\dfrac{c}{\sqrt{a^2+b^2}}\right) - \varphi, \ b < 0 \end{cases} \end{cases} \tag{13}$$

Geometric Restriction

Carryover occurs when the two rotors engage in such a way that a trapped volume is formed between them, which is isolated from both the inlet and outlet ports. This trapped volume is harmful as it leads to unnecessary compression and expansion losses. According to the fundamental law of gearing, at the point of contact, the common normal of the two conjugate curves must pass through the pitch point. If the center of curvature of L_1 lies inside the base circle, the curve's normal orientation ensures continuous conjugate action without forming an enclosed volume. Conversely, if the center of curvature of L_1 lies outside the base circle, the geometric constraints during meshing may cause the rotor profiles to form a

closed pocket before the sealing line is fully established, thereby generating a residual harmful volume. This is the geometric condition that defines the onset of carryover. Therefore, the condition for avoiding carryover can be expressed as follows [15]:

$$\begin{aligned} C_x &= x_1 + \rho_1 \boldsymbol{n}_{1x} \\ C_y &= y_1 + \rho_1 \boldsymbol{n}_{1y} \end{aligned} \tag{14}$$

Where C_x denotes the horizontal coordinate of the center of curvature and C_y denotes the vertical coordinate of the center of curvature, ρ_1 denotes the radius of curvature for L_1, x_1 and y_1 denote point (x_1, y_1) on L_1, n_{1x} and n_{1y} denote the unit normal vectors N in the horizontal and vertical coordinates, respectively. There is another way to ensure that the coordinates of the centers of the curvature circles of L_1 are all within the radius of the base circle:

$$\sqrt{C_x^2 + C_y^2} \le R \tag{15}$$

Eq. (15) expresses the distance between the center coordinate of the curvature circle and the origin is less than the radius of the base circle.

In addition to avoiding carryover, undercutting should also be avoided. Undercutting of the rotor will cause excessive clearance between the rotors and increased leakage. It also reduces the performance of the hydrogen circulating pump. To prevent undercutting, the following equation is used to determine [14]:

$$\boldsymbol{A}_1 = \begin{vmatrix} x_1^{'} & -V_{x1}^{12} \\ f_t & -f_\theta \end{vmatrix} = 0,\ \boldsymbol{A}_2 = \begin{vmatrix} y_1^{'} & -V_{y1}^{12} \\ f_t & -f_\theta \end{vmatrix} = 0 \tag{16}$$

$$\begin{cases} f_t = 2[(x_1^{'})^2 + (y_1^{'})^2 + x_1^{''}(x_1 - R\cos\theta) + y_1^{''}(y_1 - R\sin\theta)] \\ f_\theta = 2R(x_1^{'}\sin\theta - y_1^{'}\cos\theta) \\ V_{x1}^{12} = -2R\sin\theta + 2y_1, \quad V_{y1}^{12} = 2R\cos\theta - 2x_1 \end{cases} \tag{17}$$

If either A_1=0 or A_2=0 in Eq. (16) is satisfied, then it can be determined that an undercutting is occurring.

However, in practical engineering applications, it is easier to use mathematical software to solve Eq. (15), while Eq. (16) needs to be solved by numerical difference, and the solution of Eq. (16) will become difficult for the more complex rotor profiles. Therefore, in practice, we can first make the base circle radius *R* is 1, solve Eq. (15) to get the design range to avoid the carryover, and then search for the design range to avoid the undercutting in this range, and finally get the reasonable design range of the rotor profile. The specific implementation process can refer to the derivation process in Section "Conjugate Curve".

Real Profile

The real profile is corrected on the basis of the theoretical profile to ensure that there is always a uniform gap between the rotors during operation. Since the point of meshing between the rotors must make $N \cdot V = 0$, we can use the normal vector *N* of the curve L_1 to derive the actual profile. As shown in Figure 3, let R_m be the rotor radius of the theoretical profile, R_{mreal} is the rotor radius of the real profile, M is a point on the theoretical profile, O is a point on the Y axis and *OM* is the normal vector of the tangent line to the M point, Then *OM* intersects the real profile at point D. Therefore, *OD* is also the normal vector to the tangent line at point D. Thus the unit vector in the direction of *OM* is:

$$e_x = \frac{|b|}{\sqrt{a^2+b^2}}, \quad e_y = \frac{|a|}{\sqrt{a^2+b^2}} \tag{18}$$

Let the gap between the rotors is δ, then the distance between the rotor radius R_m of the theoretical profile and the rotor radius R_{mreal} of the actual profile is 0.5δ. Let the actual equation of the curve L_1 be L_{11}, and the actual equation of the curve L_2 be L_{22} then the coordinates corresponding to the actual profile are:

$$\begin{cases} E = \begin{bmatrix} \dfrac{|0.5\delta b|}{\sqrt{a^2+b^2}} \\ \dfrac{|0.5\delta a|}{\sqrt{a^2+b^2}} \\ 0 \end{bmatrix} \\ L_{11} = L_1 - E, \;\; L_{22} = L_2 + M \cdot E \end{cases} \tag{19}$$

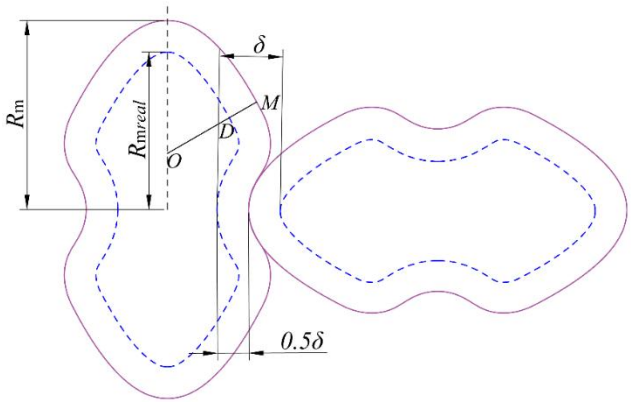

Figure 3. Real profile

DESIGN OF FOUR ROTOR PROFILES

Parabolic Rotor

As shown in Figure 4(a), the parabolic rotor consists of a parabola L_1 and its conjugate curve L_2, where L_1 is located on the outside of the base circle and L_2 is located on the inside of the base circle, and α is the angle of its envelope, which is determined by the number of lobes is denoted by z.

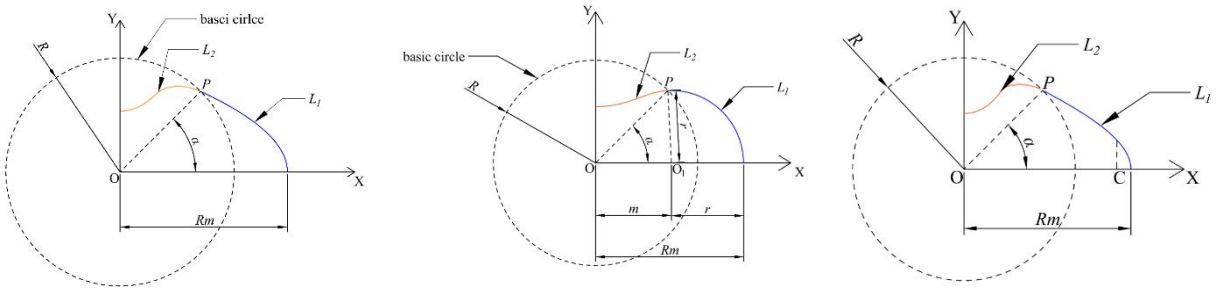

a) b) c)

Figure 4. The existing rotor profiles. (a) Parabolic rotor; (b) Circular arc rotor; (c) Hyperbolic rotor

At present, few scholars have studied parabolic rotors. In fact, parabolic rotors are good for reducing leakage of conjugate and increasing volumetric efficiency and flow rate. The parabolic profile is very simple and its parameter equation of profile can be expressed by the following equation:

$$x = \lambda R - \frac{y^2}{2k} \tag{20}$$

$$\lambda R = R_{\mathrm{m}} \tag{21}$$

Where R_{m} is the maximum rotor radius, R is the radius of the base circle, λ is defined as diameter-to-pitch ratio, k is the distance from the focus of the parabola to the directrix and k>0. To determine the value of k, it is useful to set the intersection point of the base circle with L_1 to be point P(x_{p}, y_{p}), and then the coordinates of the point P can be expressed as:

$$x_{\mathrm{p}} = R\cos\alpha, \quad y_{\mathrm{p}} = R\sin\alpha \tag{22}$$

Substituting Eq. (22) into Eq. (20) and Eq. (21) can be obtained:

$$k = \frac{R\sin^2\alpha}{2(\lambda - \cos\alpha)} \tag{23}$$

In summary, the parametric equation L_1 of the parabola is:

$$\begin{cases} L_1 = \begin{bmatrix} \lambda R - \dfrac{t^2}{2k} \\ t \\ 1 \end{bmatrix}, 0 \le t \le R\sin\alpha \\ k = \dfrac{R\sin^2\alpha}{2(\lambda - \cos\alpha)}, \quad \alpha = \dfrac{\pi}{2z} \end{cases} \tag{24}$$

Its conjugate curve L_2 can be obtained by simply substituting Eq. (24) into Eq. (13), but in order to prevent the occurrence of carryover and undercutting, it is also necessary to determine the range of values of λ. The following is an example of z=2. The curvature K and radius of curvature ρ can be easily obtained according to the knowledge of higher mathematics:

$$\begin{cases} K = \dfrac{\left|x_1'(t)y_1''(t) - y_1'(t)x_1''(t)\right|}{\left[(x_1'(t))^2 + \left(y_1'\right)^2\right]^{1.5}} \\ \rho = \dfrac{1}{K} \end{cases} \tag{25}$$

This can be obtained by simply substituting the parabola L_1 into Eq. (25) and combining Eq. (5) and Eq. (15):

$$\begin{cases} C_x = x_1 - (1+\frac{k^2}{t^2})\frac{t^2}{k} \\ C_y = y_1 - (1+\frac{k^2}{t^2})\frac{t^3}{k^2} \end{cases} \Rightarrow \begin{cases} C_x = \lambda R - \frac{t^2}{2k} - (1+\frac{k^2}{t^2})\frac{t^2}{k} \\ C_y = t - (1+\frac{k^2}{t^2})\frac{t^3}{k^2} \end{cases} \tag{26}$$

And the relationship between *k*, *λ* and *R* as well as the range of *t* can be determined by Eq. (24). For normalization purposes, the base circle radius *R* is set to unity, then the following equation can be obtained:

$$\begin{cases} C_x^2 = (\frac{1}{4k} + \frac{\sqrt{2}}{2} - k + 1)(\frac{1}{4k} + \frac{\sqrt{2}}{2} - k - 1) \\ C_y^2 = [3 + \frac{2.25t^2}{k^2} + \frac{t^4}{k^4} - \frac{3}{k}(\frac{1}{4k} + \frac{\sqrt{2}}{2})] \\ C_x^2 + C_y^2 \le 0 \\ 0 \le t \le \sin(\frac{\pi}{4}) \end{cases} \tag{27}$$

Since Eq. (27) is an implicit function, the mathematical software MATLAB can be used to plot the image and find the range of values of *k* by solving the equation. *k* must be a positive number, so the range of values of *λ* can be obtained:

$$0.708 \le \lambda \le 1.7172 \tag{28}$$

To prevent the occurrence of the undercutting phenomenon, Eq. (16) is used for the judgment. However, the Eq. (16) can be troublesome to solve, because it involves the relationship between *t* and ϑ. Therefore, a simple algorithm is designed in this paper to find the range of values of *λ*, as shown in Figure 5. It does so by first using Eq. (15) to obtain the range of values of *λ*, and then starting from the minimum value of *λ* to determine whether undercutting occurs.

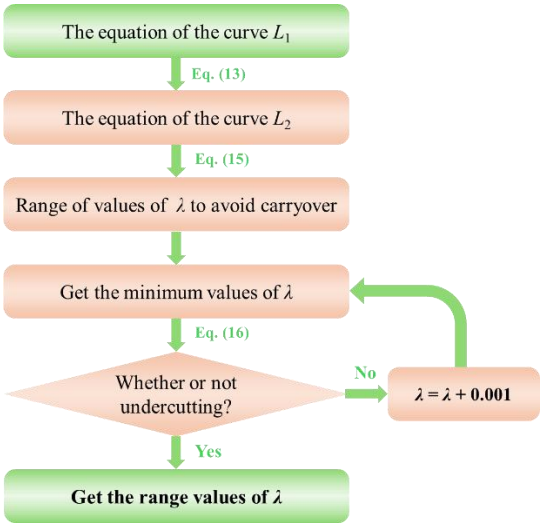

Figure 5. The method of solving for λ.

In this example, the range of λ avoid the occurrence of carryover can be obtained from Eq. (15), as shown in Eq. (28). Select λ=0.708 to substitute into Eq. (16) for the undercutting judgment, if the undercutting does not occur, then λ=λ+0.001 and then substituting into Eq. (16) for the undercutting judgment, and ultimately get λ=1.547, and then combined with Eq. (28) can be known as the range of values of λ. Similarly, when z takes different values can determine the corresponding range of values of λ:

$$\begin{cases} 0.708 \le \lambda \le 1.547, & z = 2 \\ 0.867 \le \lambda \le 1.460, & z = 3 \\ 0.924 \le \lambda \le 1.402, & z = 4 \end{cases} \tag{29}$$

Circular Arc Rotor

As shown in Figure 4(b), the circular arc rotor consists of arc L_1 and its conjugate curve L_2, arc L_1 and the base circle intersect at point P, O_1 is the center of arc L_1 and its radius is r, the distance between point O and point O_1 is m. Since the circular arc belongs to the traditional type of curve, the derivation of the arc is very mature, and will not be derived in detail, this paper directly gives the parametric equation of the circular arc L_1:

$$\begin{cases} L_1 = \begin{bmatrix} m + r\cos t \\ r\sin t \\ 1 \end{bmatrix} \left(0 \le t \le \pi - \arcsin(\dfrac{R\sin\alpha}{r}) \right) \\ m = \dfrac{(R_{\mathrm{m}})^2 - R^2}{2R_{\mathrm{m}} - 2R\cos\alpha}, \quad r = R_{\mathrm{m}} - m, \quad \alpha = \dfrac{\pi}{2z} \end{cases} \tag{30}$$

The parametric equation for L_2 can be obtained by simply substituting the above equation into Eq. (13). The solution for the range of λ is the same as parabolic rotors in Section "Conjugate Curve", and the range of λ can be solved very quickly using the algorithm shown in Figure 5.

Hyperbolic Rotor Profile

There are fewer studies on hyperbolic rotors than on parabolic rotors. Both hyperbolic and parabolic belong to conic section, therefore, the performance of hyperbolic rotor is similar to that of parabolic rotor. The parametric equation of hyperbola is:

$$\begin{cases} x = m_1 \sec t \\ y = n_1 \tan t \end{cases} \tag{31}$$

In the above equation, m_1 is the real semi-axis of the hyperbola, n_1 is the imaginary semi-axis of the hyperbola, and t is the angle, which corresponds to the hyperbola of the positive semi-axis of the X axis when t is in the first and fourth quadrants, and corresponds to the hyperbola of the negative semi axis of the X axis when t is in the second and third quadrants.

Since hyperbola has symmetrical property, the hyperbola with negative half axis of X axis is taken as an example to be studied in this paper. As shown in Figure 4(c), L_1 is a hyperbola, L_1 is obtained by translating the hyperbola of the negative axis of the X axis to the positive half-axis of the X axis, and its parametric equation can be expressed as:

$$\begin{cases} x_1 = Rm + m + m\sec t \\ y_1 = n\tan t \end{cases} \tag{33}$$

R_m in the above equation denotes the radius of the rotor of the hyperbola, and the angular range of t is in the third quadrant. Due to the point P is the intersection of L_1 with the base circle, there is:

$$\begin{cases} x_1 = R\cos\alpha, \ \ y_1 = R\sin\alpha \\ \alpha = \dfrac{\pi}{2z}, \quad \lambda = \dfrac{Rm}{R} \end{cases} \tag{33}$$

The values of m_1 and n_1 can be solved by associating Eq. (32) with Eq. (33) when t, Rm, z, and λ are given. In this paper, taking t=225° as an example, the parametric equation of hyperbola L_1 can be expressed as:

$$\begin{cases} L_1 = \begin{bmatrix} Rm + m + m\sec t \\ n\tan t \\ 1 \end{bmatrix} \\ m = \dfrac{R\cos\alpha - Rm}{1+\sec t}, \ \ n = \dfrac{R\sin\alpha}{\tan t} \\ t = \dfrac{\pi}{4} + \pi \ \ \text{(adjust value)}, \ \ \alpha = \dfrac{\pi}{2z} \end{cases} \tag{34}$$

Solving for the range of the hyperbolic λ is consistent with solving for the range of the parabola λ. It can be obtained by solving for the range of the hyperbolic λ according to what is stated in Section "Conjugate Curve" and the program shown in Figure 5. However, it should be noted that the value of t can be changed, and the range of λ corresponding to different t is not consistent and has to satisfy $m_1>n_1>0$. In this paper, we only give the range of λ when t=225°.

Novel Rotor

The novel rotor profile proposed in this paper consists of circular arcs, parabolas and their conjugate curves, in other words, the peaks of the parabolic rotor are changed to circular arcs. As shown in Figure 6(a), let the radius of the arc of the parabolic rotor be r, the center of the arc O_1 be on the X axis, and the distance between the center of the arc O_1 and the origin point O be b. The intersection of the arc with the X axis is d, and the parabola is tangent to the point S. The tangent line is made to the Y axis and the X axis respectively at the points N and M. The perpendicular line is made to the X axis over S and the point L. The radius of the

base circle is *R* and the intersection of the base circle with the *X* axis and the parabola is the point e and P. Let the coordinates of point P be (x_p, y_p), and from the geometric relationship in Figure 6(a), the following relation can be obtained:

$$\begin{cases} x_p = R\cos\alpha \\ y_p = R\sin\alpha \\ \gamma = \beta \end{cases} \tag{35}$$

According to the parabolic parametric equation of Eq. (24), the derivation of the tangent point S and using the relationship $\gamma=\beta$ can be obtained as:

$$\begin{cases} \tan\gamma = \dfrac{y_s}{k} \\ \tan\beta = \dfrac{y_s}{x_s - b} \end{cases} \Rightarrow \begin{cases} k + b = x_s \\ k = r\cos\beta \end{cases} \tag{36}$$

Since x_s is bigger than x_p, the maximum value of β can be obtained as:

$$\frac{2(Rp - R\cos\alpha)}{k} > \tan^2\beta \tag{37}$$

However, R_p is the distance from the vertex of the parabola to the origin point O. The R_m of the newly designed theoretical rotor profile should be equal to the distance from the point d to the origin O. To determine R_m in the design, it is related to R_p as follows:

$$\begin{cases} R_p - \dfrac{k(\tan\beta)^2}{2} - k + \dfrac{k}{\cos\beta} = R_m \\ \lambda_p = \dfrac{R_p}{R} \end{cases} \tag{38}$$

Thus, to determine the profile of the new type of curve, it is sufficient to be given *z*, λ_p, R_m and β. λ_p denotes the diameter-to-pitch ratio of the parabolic rotor and that β must satisfy Eq. (37). In other words, let *R*=1,

then we have $R_p=\lambda_p$, and we can determine the angular range of β from the range of λ_p in Eq. (29) and z before selecting the angular value of β.

$$\begin{cases} 0 \le \beta \le 67.171, \ z = 2 \\ 0 \le \beta \le 67.174, \ z = 3 \\ 0 \le \beta \le 68.188, \ z = 4 \end{cases} \tag{39}$$

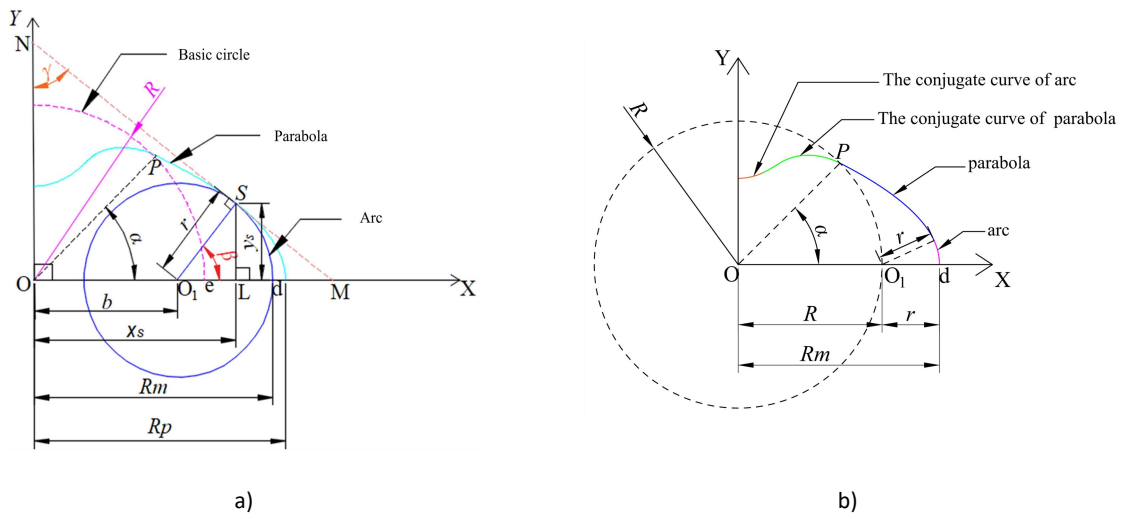

a) b)

Figure 6. Novel rotor profile. (a) Geometry of new rotor; (b) New profile of two lobes

However, the new rotor profile described above requires the relationship between the maximum radius R_p of the parabolic rotor and the maximum radius R_m of the new rotor to be established by Eq. (38), thus increasing the complexity of the design. Therefore, in this paper, for convenience, the intersection point O_1 of the base circle and the X positive semi-axis is designated as the center of the arc, then there is $b=R$, then there is $R_m=R+r$, as shown in Figure 6(b). As soon as z, λ_p and Rm are determined the other parameters can be determined, due to the following relation:

$$\begin{cases} r^2 - a^2 = 2k(\lambda_p R - k - R) \\ k = \dfrac{R\sin^2\alpha}{2(\lambda_p - \cos\alpha)} \\ R + r = R_m, \quad \alpha = \dfrac{\pi}{2z} \end{cases} \tag{40}$$

According to Eq. (40), after solving for k, r and R, the L_1 of the new rotor profile can be obtained as:

$$\begin{cases} L_1 = \begin{cases} \begin{bmatrix} R + r\cos t \\ R\sin t \\ 1 \end{bmatrix}, 0 \le t \le \beta \\ \begin{bmatrix} \lambda_p R - \dfrac{t^2}{2k} \\ t \\ 1 \end{bmatrix} (0 \le t \le R\sin\alpha) \end{cases}, \quad \beta = \arccos(\frac{k}{r}), \quad \alpha = \frac{\pi}{2z} \\ solve \begin{cases} r^2 - a^2 = 2k(\lambda R - k - R) \\ R + r = R_m \\ k = \dfrac{R\sin^2\alpha}{2(\lambda_p - \cos\alpha)} \end{cases} \Rightarrow \begin{cases} r \\ k \\ R \end{cases} \end{cases} \tag{41}$$

Since the L_1 of the new rotor profile is a combination of arc and parabola, there is a range of λ_p, which can be obtained by substituting β obtained in Eq. (39) into Eq. (36) and taking into account the relationship between k, r, and β in Eq. (23) to obtain the range of λ_p in the new rotor profile. Therefore, the range of the four rotors' λ can be found according to the method of Figure 5, as shown in Table 1.

Table 1. The range of values for λ

Type	z = 2	z = 3	z = 4
Parabolic	[0.708~1.547]	[0.867~1.460]	[0.924~1.402]
Circular arc	[1.237~1.669]	[1.120~1.477]	[1.059~1.368]
Hyperbolic	[0.708~1.518]	[0.867~1.440]	[0.924~1.380]
New	[1.375~1.547]	[1.293~1.460]	[1.236~1.402]

NUMERICAL CALCULATION STUDIES

Numerical Calculation Method

As shown in Figure7(a), the key design parameters of the rotor profile are the radius of the rotor casing (the theoretical radius of the rotor) R_m, the actual radius of the rotor R_{mreal}, the gap between the rotor and the casing is δ_1, the gap between the rotors is δ, the length of the rotor is D_1, and λ *is* R_m/R. For better comparison, this paper uses the design parameters shown in Table 2, as shown in Figure 7(b). It should be

noted that a comprehensive multi-objective optimization for each rotor type would entail a substantial workload, which lies beyond the scope of the present study. Therefore, to ensure a fair comparison, consistent geometric parameters were adopted for all four rotor profiles, while guaranteeing interference-free operation under geometrically feasible conditions. A two-lobe Roots pump was selected for the numerical simulation study, with the λ set to 1.5—a value lying within the intersection of the feasible ranges of all four profile types. Furthermore, λ=1.5 is a commonly adopted diameter-to-pitch ratio in industrial applications, thereby enhancing the engineering relevance of the conclusions drawn from this study.

Table 2. The geometric parameters of the model

Type	D_1(mm)	R_m(mm)	R_{mreal}(mm)	δ_1(mm)	λ	δ(mm)
Parabolic	60	33	32.9	0.1	1.5	0.1
Circular arc	60	33	32.9	0.1	1.5	0.1
Hyperbolic	60	33	32.9	0.1	1.5	0.1
New rotor	60	33	32.9	0.1	1.5	0.1

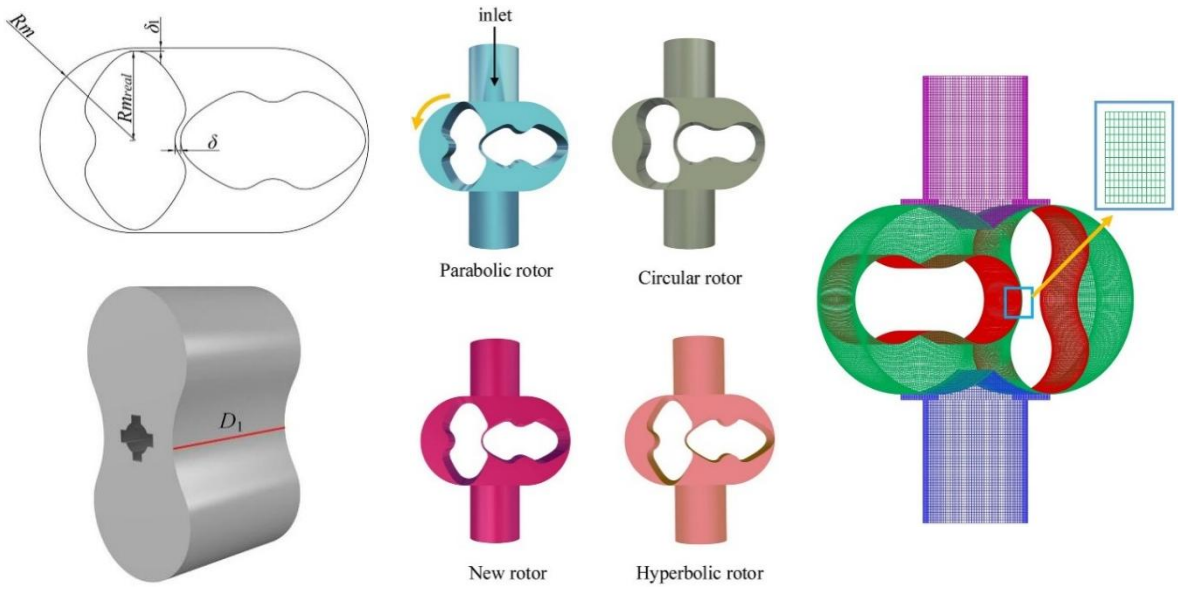

Figure 7. Pre-processing. (a) Geometric parameters of the rotor; (b) The models of Four rotors; (c) Grid of rotor

As a professional CFD software, Pumplinx is especially good at numerical calculations of rotating machinery. It has been successfully used to compare simulation and experimental results. Therefore, this paper adopts Pumplinx to construct the fluid analysis model. Firstly, the coordinate points of Matlab are imported into Catia and generate the model, and then the model is converted into STL format and imported into Pumplinx, then add the mesh of the front and back cover plates, as shown in Figure 7(c).

Pumplinx has a meshing template for Roots pumps, so its meshing is extremely easy. Set the gas as an ideal gas and set the dynamic viscosity to 8.93847e-06(Pa-s), the heat conductivity to 0.1867(W/(m·K)) and the specific heat capacity to 14312.8(J/kg·K). The Realizable k-ε turbulence model was selected. The inlet pressure was set to one atmosphere and the pressure ratio was 1.1. The speed was set to 6000 RPM. In addition, a grid independence study was conducted using five different mesh resolutions: 1.0, 1.5, 2.1, 3.0, and 3.9 million elements. The results indicate that the predicted flow rate of the Roots pump increases with mesh refinement but plateaus beyond 2.1 million elements. The relative error between the solutions obtained with 2.1 million and 3.9 million elements is merely 0.199%. Considering the trade-off between computational accuracy and time cost, a mesh with 2.1 million elements was adopted for all subsequent numerical simulations in this study.

To verify the accuracy of the numerical calculations, This paper uses the experimental data and model in Reference [19] to verify the accuracy of the simulation through Pumplinx. As shown in Figure 8, the absolute error between the simulation results and the experimental data remained within 1.05% for pressure ratios of 1.1 and 1.2. In contrast, the error increased significantly to 7.86% at a pressure ratio of 1.3. The numerical method established in this paper may overestimate the leakage losses, resulting in increased errors in the calculated results. The pressure ratio of a Roots pump is a critical design and operational parameter in hydrogen fuel cell applications, as it significantly influences volumetric efficiency. For instance, when the pressure ratio increases from 1.1 to 1.2, the volumetric efficiency of air decreases by 7%, whereas that of hydrogen drops sharply by 29% [6]. Due to the low viscosity of hydrogen, even a small increase in the pressure ratio can cause a sharp rise in internal leakage. Considering both simulation accuracy and practical operating conditions, the pressure ratio of 1.1 was selected for the subsequent numerical simulations in this study.

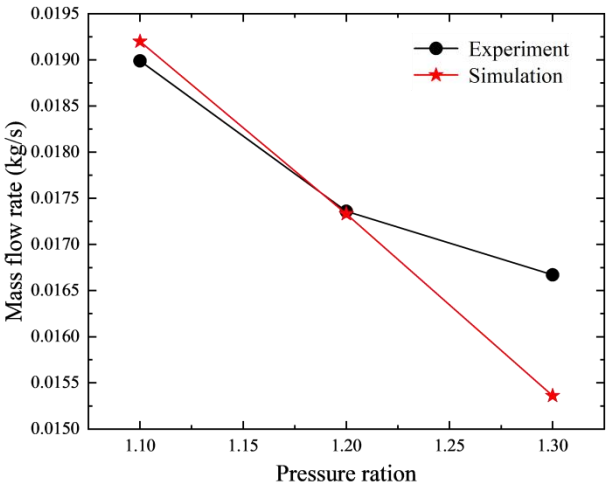

Figure 8. Verify the accuracy of numerical calculations

Results

In the fuel cell systems, the hydrogen circulating pump not only has high volumetric efficiency, but also has to minimize the pulsation to avoid noise generation. Therefore, this paper chooses flow pulsation coefficient and volumetric efficiency as indicators to evaluate the performance of four rotors. The flow pulsation coefficient is related to the smoothness of the flow rate, and the volumetric efficiency is related to the ability of the pump to resist leaks. The formulas for flow pulsation coefficient and volumetric efficiency are as follows:

$$\begin{cases} f_Q = \dfrac{V_{\max} - V_{\min}}{V_{\text{ave}}} \\ \eta_V = \dfrac{Q_{\text{out}}}{Q_{\text{th}}} \end{cases} \tag{42}$$

Where f_Q denotes the flow pulsation, V_{max}, V_{min} and V_{ave} denote the maximum volumetric flow rate, minimum volumetric flow rate and average volumetric flow rate respectively. η_v denotes the volumetric efficiency, Q_{out} denotes the actual output flow rate, and Q_{th} denotes the theoretical output flow rate. Q_{out} is represented by the simulation results of Pumplinx, and Q_{th} is calculated as follows:

$$Q_{\mathrm{th}} = 2\varsigma\pi(R_{\mathrm{m}})^2 D_1 n \tag{43}$$

Where n is the rotational speed and ς denotes the area utilization factor, which is calculated as follows:

$$\varsigma = \frac{\pi(R_{\mathrm{m}})^2 - S_{\mathrm{rotor}}}{\pi(R_{\mathrm{m}})^2} \tag{44}$$

Here S_{rotor} represents the area of a single rotor, as shown in Table. 3. Substituting the data from Table 3 into Eq. (43) to obtain Q_{th}.

Table 3. Theoretical volumetric flow rate

Type	Area of a single rotor (mm^2)	Q_{th} (m^3/h)
Parabolic	1594.71	78.908
Circular arc	1666.84	75.790
Hyperbolic	1581.98	79.455
New	1675.72	75.405

According to the results of simulation we can get the flow rate of parabolic rotor, circular arc rotor, hyperbolic rotor and new type of rotor, respectively, as 42.76 m^3/h, 37.61 m^3/h, 42.35 m^3/h and 41.89 m^3/h, as shown in Table 4. It is evident that the circular arc rotor exhibits the lowest flow rate. The flow rate variations of the hyperbolic, parabolic, and new rotors are comparable. The flow pulsation coefficients f_Q of the four rotors can be obtained according to Eq. (42). Results indicate that the new rotor design exhibits the lowest flow pulsation and consequently, the smoothest flow output. In contrast, the circular arc rotor demonstrates the highest flow pulsation and the lowest flow rate. Furthermore, the new rotor achieves the highest volumetric efficiency and the lowest leakage. Although the new rotor's flow rate is only 2.05% lower than that of the parabolic rotor, its flow pulsation coefficient is reduced by 5.5%, and its volumetric efficiency is improved by 2.51%. These results demonstrate the reliability of the proposed novel rotor for use in hydrogen circulating pumps.

Table 4. Parameters of performance for four rotors

Type	f_Q	Q_{out} (m^3/h)	η_v (%)
Parabolic	0.57	42.76	54.19
Circular arc	0.65	37.61	49.62
Hyperbolic	0.58	42.35	53.30
New	0.54	41.89	55.55

Discussion

Since the pressure distribution of the four rotor profiles is not particularly obvious under the pressure ratio of 1.1. Therefore, to better compare the performance of the four rotor profiles, velocity contour is used in this paper to observe the internal flow characteristics of the four rotors.

As shown in Figure 9, at 18°, the leakage at the gap between the Circular arc rotor [Figure 9 a)] and the casing is the largest, and a large amount of gas at the outlet flows directly back into the pump chamber through the casing gap and collides with the outflow gas and forms a vortex at the region (I). The other three rotor profiles [Figure 9 b)-d)] also have leakage at the gap between the casing and rotor, and form vortices at region (I), but the reasons for their formation of vortices at region (I) are not due to backflow of gas. The circular arc rotor also forms a vortex in the region (II), but the other three rotor profiles do not have this phenomenon. This indicates that the circular arc rotor also has the largest conjugate leakage. In addition, the velocity fluctuation of the arc rotor is large in region (III), which may be due to the fact that the rotor profile is not concave enough at the valley of lobe.

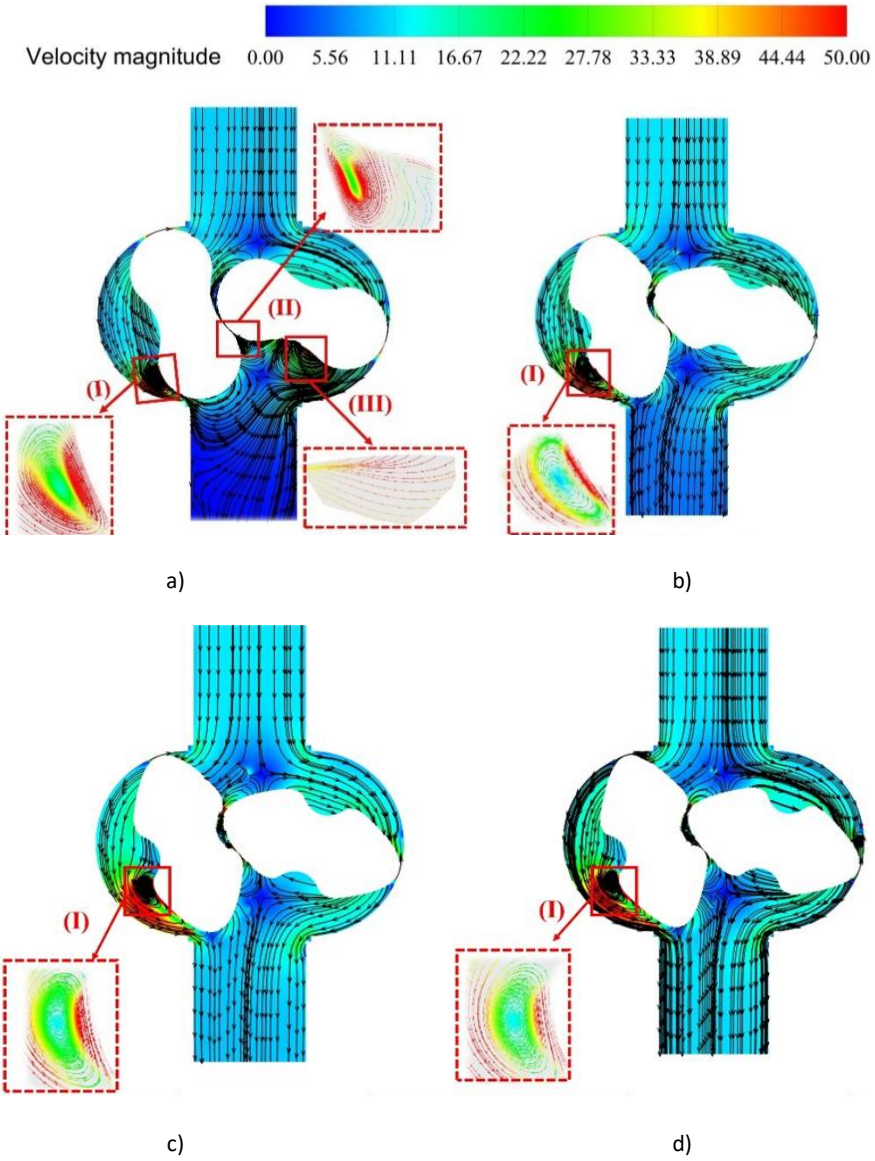

Figure 9. Rotation angle of 18°. (a) Circular arc rotor; (b) New rotor; (c) Parabolic rotor; (d) Hyperbolic rotor

As shown in Figure 10, at 36°, vortices appear in regions (I), (IV), (V), and (VI) for the arc rotor [Figure 10 a)], while the other three rotors [Figure 10 b)-d)] have vortices only in regions (I) and (IV). The reason for the vortex in regions (IV) for the four rotors is that the gas at the inlet tries to pass through the gap between the rotors, due to the small gap, the gas hits the wall of the rotor and forms a vortex. Therefore, the larger the vortex, the smaller the leakage of the gap between the rotors. From Figure 10, it can be obtained that the conjugate leakage of the arc rotor is the largest.

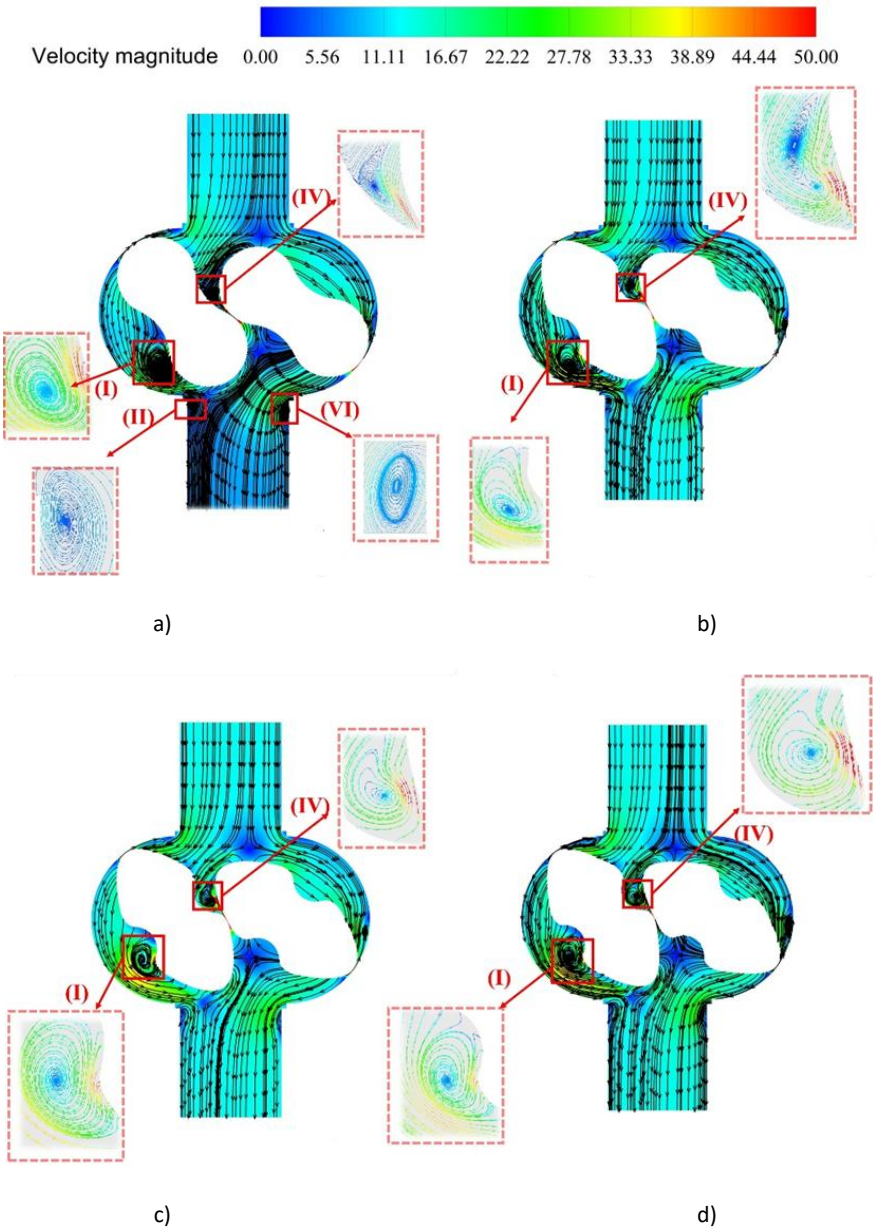

Figure 10. Rotation angle of 36°. (a) Circular arc rotor; (b) New rotor; (c) Parabolic rotor; (d) Hyperbolic rotor.

As shown in Figure 11, at 54°, the vortices formed by the four rotors in region (I) are in the opposite direction to the vortices at 18°and 36°. The new rotors [Figure 11 b)], parabolic rotor [Figure 11 c)] and hyperbolic rotor [Figure 11 d)], have larger vortices in region (IV) and vortices in regions (V) and (VI). The vortex of the arc rotor [Figure 11 a)] becomes smaller in region (VI). The vortices of the new type rotor are the largest in the regions (V) and (VI), and the vortex of the hyperbolic rotor is larger in the (VI) region. Meanwhile, the vortex in region (I) is never eliminated and its position is always near the joint of L_1 and L_2.

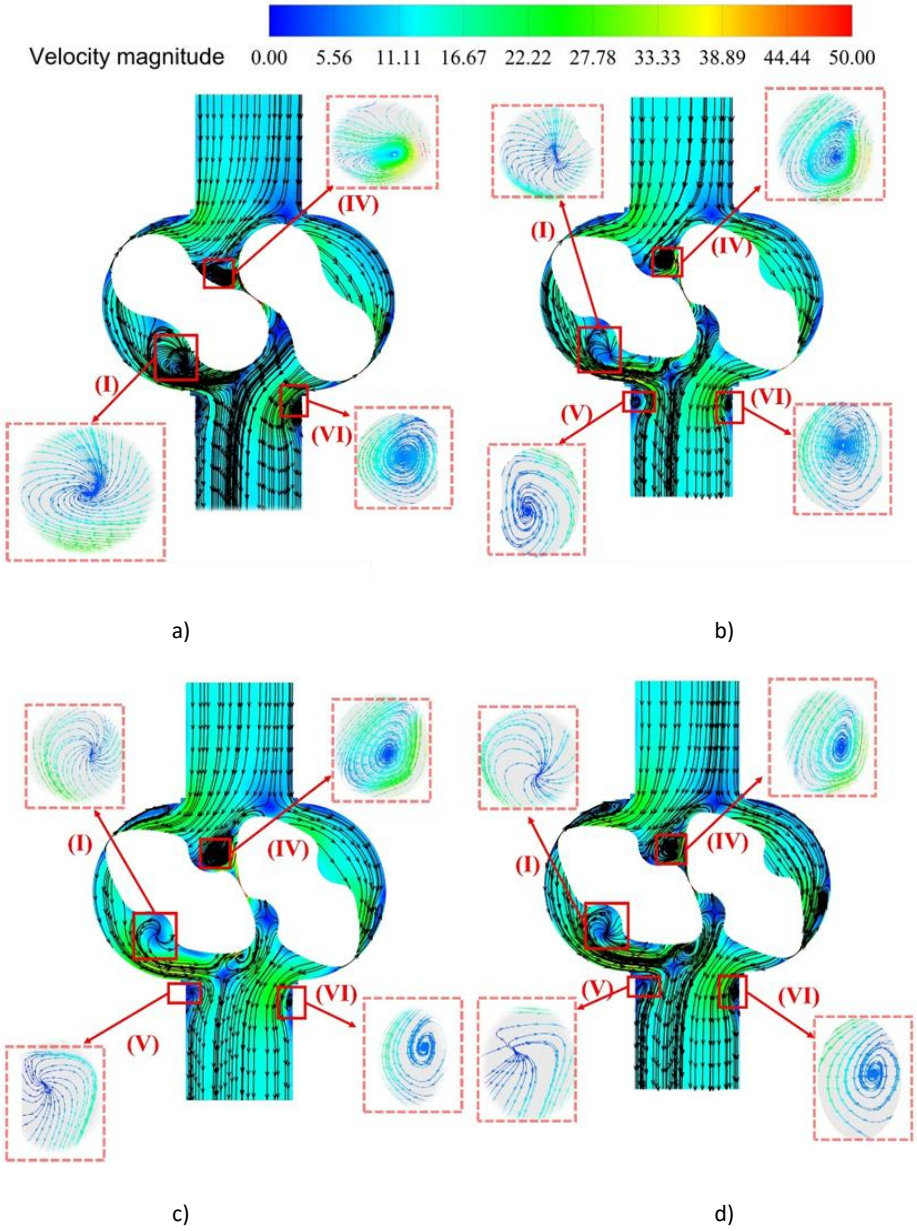

Figure 11. Rotation angle of 54°. (a) Circular arc rotor; (b) New rotor; (c) Parabolic rotor; (d) Hyperbolic rotor

As shown in Figure 12, at 72°, the parabolic rotor [Figure 12 c)] has the largest vortex in region (IV), followed by the circular arc rotor [Figure 12 a)]. Meanwhile, the vortex of hyperbolic rotor [Figure 12 d)] and new type rotor [Figure 12 b)] is weakened in region (IV). For the arc rotor, with the rotation of the rotor, the gas at the rotor gap is carried to the inlet by the rotor and collides with the gas at the inlet to form a vortex. At the same time, the turbulence caused by the gas at the inlet hitting the rotor wall near the vortex in region (IV) intensifies the vortex speed. However, the vortices of the other three profiles in region (IV) are significantly weakened. The reason is that their lobe valleys are concave, and the return flow caused by

the gas hitting the lobe valleys needs to climb for some distance. This indicates that the design of rotor profiles should not only take into account the leakage of gaps, but also take into account the problem of weakening the vortex, because the generation of vortex not only affects the normal flow of the gas, but also affects the volumetric efficiency of the pump and the flow pulsation.

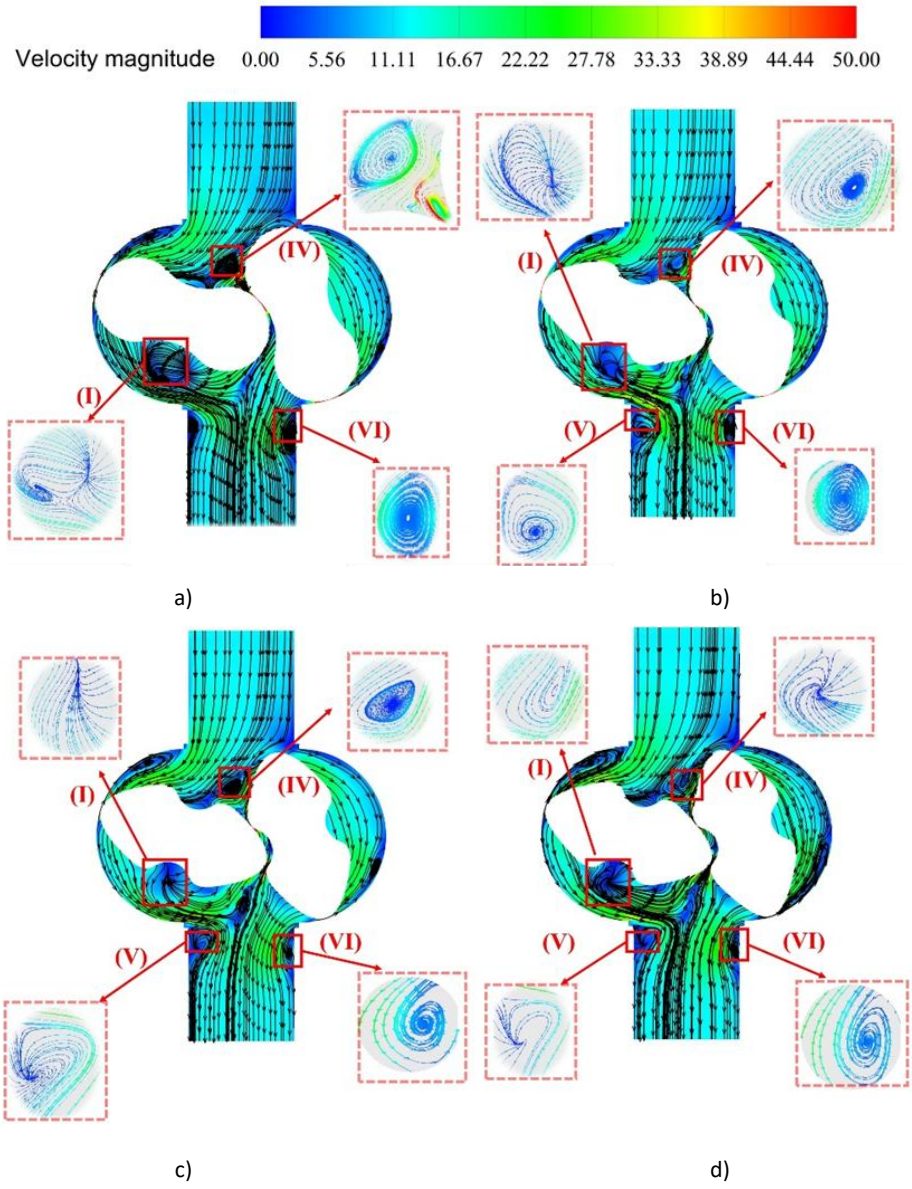

Figure 12. Rotation angle of 72°. (a) Circular arc rotor; (b) New rotor; (c) Parabolic rotor; (d) Hyperbolic rotor

CONCLUSIONS

Building upon previous research, this study summarizes a new design methodology for Hydrogen circulating Roots pumps. Then, based on the geometrical constraints of conjugate profiles, a new method is presented to determine the feasible range of the design parameter λ for engineering applications. A novel rotor profile, composed of circular arcs and parabolic segments, is proposed. The main contributions of this paper are as follows:

(1) A new general design formula is derived for generating rotor profiles. This formula enables the efficient construction of various profiles, including the circular arc, parabolic, hyperbolic, and the proposed novel rotor. The novel rotor profile combines circular arcs, parabolic segments, and their corresponding conjugate curves.

(2) A practical method for determining the feasible range of λ, based on the geometrical constraints of conjugate rotor profiles, is proposed for engineering use. This method was applied to determine the λ ranges for the four investigated rotor profiles.

(3) The circular arc rotor exhibits the largest flow pulsation and the lowest volumetric efficiency. The parabolic rotor achieves the highest flow output. It also demonstrates higher volumetric efficiency and lower flow pulsation than the circular arc rotor. The new rotor exhibits a flow rate comparable to that of the parabolic rotor, while achieving the highest volumetric efficiency (55.55%) and the lowest flow pulsation (0.54) among all compared profiles. These results confirm the superior overall performance of the proposed novel rotor.

(4) Flow field analysis revealed that hydrogen readily forms vortices at the junction between the L1 and L2 profile segments. The intensity and scale of the vortices are the primary factors contributing to flow pulsation.

The improved volumetric efficiency and reduced flow pulsation achieved by the novel rotor provide a more stable power foundation for hydrogen-driven systems. Such technical enhancements hold potential reference value for the operational reliability of green energy power systems in various industrial sectors, including textile manufacturing, thereby supporting the broader transition toward sustainable, low-carbon production.

Author Contributions

Conceptualization – Wu Z and Lin R; methodology – Wu Z and Qi P; formal analysis – Zhang L; investigation – Lin R and Qi P; writing-original draft preparation – Wu Z and Qi P; writing-review and editing – Lin R and Zhang L. All authors have read and agreed to the published version of the manuscript.

Conflicts of Interest

The authors declare no conflict of interest.

Funding

This research received no external funding.

Data Availability Statement

The data presented in this study are available on request from the corresponding author.

REFERENCES

[1] Dehshiri SSH, Firoozabadi B. Solar to power and hydrogen production, storage and utilization in textile industry: A feasibility analysis. Applied Energy. 2024; *362*, 122956. doi. 10.1016/j.apenergy.2024.122956

[2] Kipchumba BB, Chemweno P, Ochola J, Nganyi EO. Statistical mapping and data collection of critical equipment failures in the weaving section of textile manufacturing. Engineering Reports. 2024; 6(3), e12743. doi. 10.1002/eng2.12743

[3] Alıcı H, Yiğit BN, Menemencioğlu B, Tümay Ateş K, Demirdelen Ö, Demirdelen T, Kıvanç Z. Analysis of carbon footprint including process-level calculation and its influencing factors of process for low-carbon and sustainable textile industry. Sustainability. 2024; 16(23), 10168. doi.org/10.3390/su162310168 International Journal of Hydrogen Energy.

[4] Dehshiri SSH, Firoozabadi B. Hydrogen penetration in textile industry: A hybrid renewable energy system, evolution programming and feasibility analysis. Energy. 2025; 318, 134785. doi.org/10.1016/j.energy.2025.134785

[5] Singla MK, Nijhawan P, Oberoi AS. Hydrogen fuel and fuel cell technology for cleaner future: a review. Environmental Science and Pollution Research. 2021; 28(13), 15607-15626. doi.org/10.1007/s11356-021-13191-3

[6] Xing WS, Zhang F, Song JL, Chen K, Yuan SQ, Zhu XM. Design and transient flow analysis of a new rotor profile for hydrogen circulating pumps. *Fuel*. 2026; *407*:137447. doi. 10.1016/j.fuel.2025.137447

[7] Liang X, Kang H, Shen J, Li Z, Zeng R. Review and analysis of hydrogen recirculation devices for compact vehicular proton exchange membrane fuel cells. Journal of Power Sources. 2023; 555:232308. doi. 10.1016/j.jpowsour.2022.232308

[8] Qi PH, Wu ZX, Mou JG, Wu DH, Gu YQ, Xu MS, Luo, Y. A review of water management in proton exchange membrane fuel cell systems. Sustainable Energy & Fuels. 2025; 9(1), 72-97. doi.org/10.1039/D4SE01020E

[9] Wang PY, Fong ZH, Fang HS. Design constraints of five-arc Roots vacuum pumps. Proceedings of the Institution of Mechanical Engineers, Part C: Journal of Mechanical Engineering Science. 2002; 216(2):225–234. doi. 10.1243/0954406021525151

[10] Xing LF, Feng JM, Chen WQ, Xing ZY, Peng XY. Development and testing of a roots pump for hydrogen recirculation in fuel cell system. Applied Sciences. 2020; 10(22):8091. doi. 10.3390/app10228091

[11] Wu YR, Tran VT. Generation method for a novel Roots rotor profile to improve performance of dry multi-stage vacuum pumps. Mechanism and Machine Theory. 2018; 128:475–491. doi. 10.1016/j.mechmachtheory.2018.06.009

[12] Tran VT, Thanh BT, Long BT, Tuan HQ, Nguyen DT. Study on the effects of tooth profile design parameters of rotor to performance of vacuum pump. International Journal of Modern Physics B. 2020; 34(22n24):2040141. doi. 10.1142/s0217979220401414

[13] Wang J, Liu RQ, Yang SR, Li HX, Wang ZL, Li Q. Geometric study and simulation of an elliptical rotor profile for Roots vacuum pumps. Vacuum. 2018; 153:168–175. doi. 10.1016/j.vacuum.2018.04.014

[14] Hsieh CF. A new curve for application to the rotor profile of rotary lobe pumps. Mechanism and Machine Theory. 2015; 87:70–81. doi. 10.1016/j.mechmachtheory.2014.12.018

[15] Hwang YW, Hsieh CF. Study on high volumetric efficiency of the Roots rotor profile with variable trochoid ratio. Proceedings of the Institution of Mechanical Engineers, Part C: Journal of Mechanical Engineering Science. 2006; 220(9):1375–1384. doi. 10.1243/09544062jmes176

[16] Singh G, Sun S, Kovacevic A, Li QH, Bruecker C. Transient flow analysis in a Roots blower: Experimental and numerical investigations. Mechanical Systems and Signal Processing. 2019; 134:106305. doi. 10.1016/j.ymssp.2019.106305

[17] Wei H, Xing L, Wang B, Feng J, Peng X. 3D transient numerical simulation of a helical roots air compressor for FCVs. Proceedings of the Institution of Mechanical Engineers, Part C: Journal of Mechanical Engineering Science. 2021; 235(23):7287–7298. doi. 10.1177/09544062211014543

[18] Zhai H, Li W, Ji LL, Li S, Cao YH, Li YK. Research on measurement method for high-frequency pulsation flow of hydrogen circulating pump. International Journal of Hydrogen Energy. 2023; 48(39):14853–14865. doi. 10.1016/j.ijhydene.2022.12.358

[19] Zhou R, Dong L, Liu HL, Dai C, Zhang LX. Excitation characteristics of lobe hydrogen circulating pump in polymer electrolyte membrane fuel cell under different clearances and pressure ratios. Applied Thermal Engineering. 2023; 226:120230. doi. 10.1016/j.applthermaleng.2023.120230

[20] Dong L, Zhou R, Liu HL, Zhang LX, Dai C, Mao YH, Hu JB. Effect of rotational speed on unstable characteristics of lobe hydrogen circulating pump in fuel cell system. International Journal of Hydrogen Energy. 2022; 47(50):21435–21449. doi. 10.1016/j.ijhydene.2022.04.248

[21] Li S, Li W, Ji LL, Zhai HL, Li YK, Wang C, Li XY. Effect of pressure ratio on transient flow in hydrogen circulating pump. International Journal of Hydrogen Energy. 2023; 48(69):26937–26950. doi. 10.1016/j.ijhydene.2023.03.370